## PAPER

Check for updates

# Solid-state NMR reveals mixed side-chain organization across pores in amphiphilic covalent organic frameworks

Simona Bassoli,[a] Alexey Krushelnitsky, [b] Farzad Hamdi,[cd] Jonas Lührs,[a] Panagiotis L. Kastritis,[cde] Daniel Sebastiani, [a] Kay Saalwächter [*b] and Frederik Haase [*a]

Covalent organic frameworks (COFs) are a promising class of materials for advanced applications due to their well-organized backbone and pores. Amphiphilic side chains that are prone to self-organization by phase separation are envisioned to lead to chemically heterogeneous pores with distinct microenvironments having varying philicities. Previously, these microenvironments were only indirectly investigated and thus the microphase separation in COFs has remained inconclusive. We probe the local structure of a dual-chain functionalized, amphiphilic COF where the pore size and side chain length are expected to lead to through-pore interactions. $^{13}C$ and $^{1}H$ MAS NMR experiments, including 2D $^{1}H$–$^{1}H$ spin-diffusion exchange, proved that close spatial proximity and dynamic interactions between the chemically different side chains exist for a majority of the side chains, excluding the possibility of significant phase separation. These results indicate that a mixed arrangement in which polar and non-polar chains coexist within the same pores predominates. Our study demonstrates the power of ssNMR in elucidating the structure of amphiphilic COFs at the molecular level and provides new insights into the design of frameworks with chemically heterogeneous pores.

*Frederik Haase is a tenure-track Junior Professor at Martin-Luther-University Halle-Wittenberg, where he also leads a research group funded by the Emmy-Noether-Program. His research centers on linker-centric design strategies in COFs and MOFs, with a particular focus on topology control, geometric frustration, and new pathways to crystalline covalent materials. Before, he held group leader positions at Karlsruhe Institute of Technology as a Liebig Fellow, and completed postdoctoral research at Kyoto University as a JSPS Fellow. He obtained his PhD in 2018 at the Ludwig-Maximilians-University of Munich and the Max Planck Institute for Solid State Research in the group of Bettina Lotsch.*

**Frederik Haase**

## Introduction

The synthesis and characterization of crystalline porous covalent organic frameworks (COFs) has attracted continued interest due to their chemical versatility and structural predictability.[1] COFs have shown great potential in catalysis,[2–4] gas separation,[5,6] energy storage and conversion,[7,8] selective adsorption,[9–11] and drug delivery.[12] These framework materials are synthesized and at the same time crystallized through the process in which building blocks self-assemble *via* the combination of dynamic covalent bonds, which can reversibly form and break under synthesis conditions, and non-covalent interactions.[13,14]

While much research has focused on optimizing the reversible covalent bond formation during crystallization, additional weak non-covalent interactions have emerged as critical factors influencing the structure and crystallinity of COFs. These interactions, including hydrogen bonding,[15,16] steric effects,[17] π–π stacking and van der Waals forces,[18–20] play

*aInstitute of Chemistry, Martin-Luther-Universität Halle-Wittenberg, Halle/Saale, Germany. E-mail: frederik.haase@chemie.uni-halle.de*

*bInstitute of Physics, Martin-Luther-Universität Halle-Wittenberg, Halle/Saale, Germany. E-mail: kay.saalwaechter@physik.uni-halle.de*

*cDepartment of Integrative Structural Biochemistry, Institute of Biochemistry and Biotechnology, Martin Luther University Halle-Wittenberg, Halle/Saale 06120, Germany*

*dBiozentrum and ZIK HALOmem, Martin Luther University Halle-Wittenberg, Halle/Saale 06120, Germany*

*eInstitute of Chemical Biology, National Hellenic Research Foundation, Athens, 11635, Greece*

This journal is © The Royal Society of Chemistry 2026

*J. Mater. Chem. A*, 2026, **14**, 1647–1656 | **1647**

a crucial role in determining the COF structure. These non-covalent forces can be strategically employed to direct the stacking and alignment of COF layers.[21,22] Beyond the structure-directing capabilities,[23,24] functional groups also inherently functionalize COF pores.[25] This dual role has been essential in imparting tailored functionality to COFs, especially since their backbone and pore structures are more limited compared to other porous materials like metal–organic frameworks.

One effective strategy for functionalizing COFs involves attaching flexible side chains to the organic building blocks, allowing for modification of the internal pore environment. This approach has been successfully applied to enhance ionic conductivity,[26,27] impact on photocatalytic synthesis,[28,29] promote COF exfoliation,[30] and to adjust the affinity for guest molecules.[31] Nevertheless, a pore environment may not be ideal for applications that require simultaneous interaction with both hydrophilic and hydrophobic species, such as dual drug delivery,[32] selective separation,[33] or multiphase catalysis.[34]

Addressing this limitation, amphiphilic COFs with hetero-environmental pores have emerged as a promising class of materials.[35,36] These frameworks incorporate linkers with at least two side chains with different polarities, typically hydrophilic and hydrophobic, that are expected to spontaneously self-sort within the pores. This self-organization of amphiphilic materials minimizes the system's free energy and results in the spatial segregation of chemically distinct domains with alternate hydrophilic and hydrophobic regions.[37–39] As a result, if phase separation and heterogeneous microenvironments are achieved, amphiphilic COFs would offer an attractive platform for advanced applications, including Janus-type membranes,[36] the targeted delivery of both hydrophilic and hydrophobic compounds,[35] and fundamentally as an additional tool to increase the structural complexity in COFs.

Despite the conceptual appeal, direct evidence for phase separation in amphiphilic COFs is limited. Recently, Jiang et al.[36] reported the synthesis of two-dimensional COFs based on an amphiphilic linker with a hydrophobic butyl, phenyl or naphthyl chain on one side and a hydrophilic hydroxyl group on the other, where a steric hindrance based mechanism was suggested for the hydrophilic and hydrophobic microphase separation in a specific kgm COF. In the case of phase separation or specific orientation of the side groups, hydroxyl groups would be located in smaller trigonal micropores, while hydrophobic side chains would be found in larger hexagonal pores. In their work, the formation of the kgm net instead of the sql net was offered as proof that microphase separation had occurred. Ji et al. described the synthesis and study of a COF based on a linker with an aliphatic heptyl and a hydrophilic monomethyl diethylene glycol side chain.[35] In their work, they argued for microphase separation based on experimental evidence from nitrogen isotherms and derived pore distributions.[35] However, these indirect techniques offer no definitive conclusions regarding the local pore environment.

This highlights the need to conclusively prove or disprove the phase separation in amphiphilic COFs through direct experimental evidence. Diffraction techniques such as TEM and PXRD are, in principle, suitable for investigating both the local and long-range order of pores, provided that a sufficient degree of phase separation occurs. However, for these techniques to reveal distinct pore environments, the electron density and its distribution must differ consistently between hydrophilic and hydrophobic microdomains. Additionally, the relatively poor crystallinity of COFs further complicates such analyses.

In light of these limitations, solid-state nuclear magnetic resonance spectroscopy (ssNMR) has emerged as a powerful complementary tool for studying the local chemical environment in porous materials, including MOFs and COFs.[40–46] ssNMR is particularly valuable because it can provide information that other methods cannot achieve with the same accuracy. Previous studies have demonstrated that ssNMR can analyze the chemical environment,[40,42] linker arrangements,[42] dynamics,[43,47,48] as well as atomic connectivity providing insights into pore organization in reticular materials.[40,43,44] Atomic level analysis by ssNMR also clarifies interactions between guests and the porous matrix.[40,42,43] In particular, ssNMR was used to investigate the side-chain mobility in porous zirconium-based MOFs.[49] Application of advanced 1D and 2D techniques, such as cross-polarization (CP) and dipolar-coupling chemical-shift correlation (DIPSHIFT), allowed the quantification of flexibility and architecture of the side chains within the framework. Additionally, ssNMR was used to probe the dynamics of polymer chains confined in nanochannels and revealed how confinement affects chain behavior and interactions with the material surface.[48]

Here, we designed and synthesized a square-lattice COF from a linear amphiphilic linker featuring a terephthalaldehyde core with a hydrophilic monomethyl triethylene glycol (EG) chain and a hydrophobic decyl alkyl group, combined with a tetrafunctional porphyrin tetraamine node linker (5,10,15,20-tetrakis(4-aminophenyl)-21H,23H-porphyrin, TAPP). Compared to previous amphiphilic COFs,[35] our design features smaller pores with side chains of much longer length, increasing the probability of side chain interactions and potential phase separation.

We employed ssNMR spectroscopy to explore the spatial configuration of side chains inside COF pores, testing whether hydrophilic and hydrophobic groups organize into distinct microenvironments. ^{13}C and ^{1}H MAS NMR methods were used to identify different chemical environments and confirm the constrained mobility of the side chains. Proton spin diffusion experiments showed magnetization transfer between EG and alkyl chain as well as framework proton sites, with 2D [1]H–[1]H spin-diffusion exchange spectra (corresponding to the solution-state NOESY experiment) at different mixing times revealing clearly that protons from both side chains are spatially close and interact through signal exchange. These results suggested that the majority of chains are intermixed and that if phase separation occurs, it is only in a small fraction. Together, these insights form the basis for understanding how amphiphilic side chain arrangements influence local environments, structural disorder, and ultimately the emergent properties of these materials.

**1648** | J. Mater. Chem. A, 2026, **14**, 1647–1656

This journal is © The Royal Society of Chemistry 2026

# Results

## Materials synthesis

The amphiphilic COF linker $C_{10}EG_3TA$ building block was synthesized from 2,5-dihydroxyterephthalaldehyde, following a two-step process: monoalkylation with 1-bromodecane, followed by alkylation with diethylene glycol 2-bromoethyl methyl ether (Fig. S1). This resulted in a linker, where the amphiphilicity arises from the presence of a hydrophobic aliphatic chain and a hydrophilic oligoethylene glycol chain. This linker was then used for the synthesis of the imine-based $C_{10}EG_3TA$-COF, by combining it with 5,10,15,20-tetrakis(4-aminophenyl)-21$H$,23$H$-porphyrin (TAPP) under solvothermal conditions (Fig. 1). After the reaction, the precipitated COF was filtered, thoroughly washed with methanol, subjected to Soxhlet extraction with methanol, and finally activated using supercritical $CO_2$. The COF synthesis was optimized with the highest crystallinity being obtained for a 9:1 mixture of 1-butanol and 1,2-dichlorobenzene with 6 M acetic acid (Fig. S2). These synthesis conditions were very similar to those used by Ji *et al.*[35] for their terphenyl based amphiphilic linker, where they claimed the formation of hetero-environmental pores.

## Structural characterization

The high-resolution synchrotron X-ray diffraction pattern of $C_{10}EG_3TA$-COF showed five prominent reflections in the low $q$ region and one broad reflection in the high $q$ region of the PXRD diffractogram. The most intense peaks appeared at 0.247 and 0.267 Å$^{-1}$, while weaker reflections were observed at 0.364, 0.494 and 0.537 Å$^{-1}$ (Fig. 2 and S3).

A unit cell model was constructed based on the geometries of the precursor building blocks and their expected connectivity in a square lattice topology (*sql*) and then was geometry optimized using force fields. Simulated PXRD patterns based on this *sql* structural model with AA stacked arrangements matched the observed PXRD well, but could not explain the split reflection at low angle, which was however described well by a model showing slip stacking. The AB stacking model, characterized by
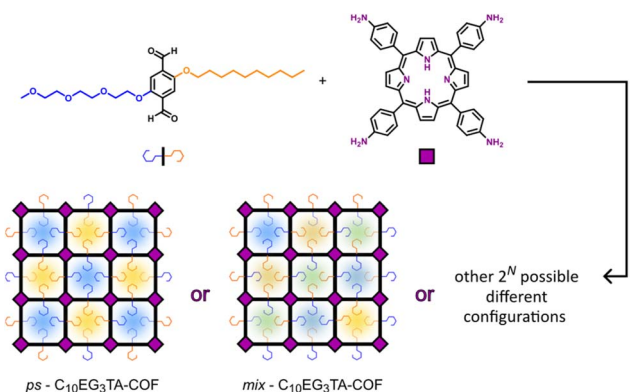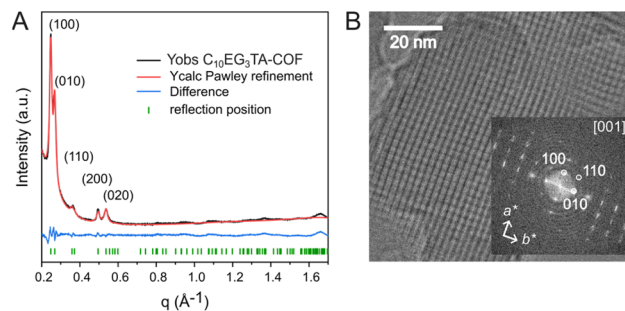


**Fig. 2** (A) X-ray powder diffraction (XRPD) pattern (black) of the synthesized sample compared with the calculated pattern (red) and their difference (blue). Green vertical ticks indicate the Bragg reflection positions of the reference phase. (B) High-resolution transmission electron microscopy (HRTEM) image showing well-ordered square lattice arrangement, confirming the crystallinity of the sample. The inset shows the corresponding fast Fourier transform (FFT) pattern along the [001] zone axis, with indexed diffraction spots.

a staggered configuration between layers, was excluded due to its poor agreement with the experimental data (Fig. S6).

Based on the AA stacking structural model, two distinct side chain configurations were constructed, differing in the organization of the side chains within the pores (Fig. 3). For each site of the amphiphilic linker in the COF lattice, two orientations were possible during crystallization. The linker is fixed in position by the COF lattice, but also by the $\pi$–$\pi$ stacking with the next layer. Due to the nonsymmetric substitution of the linker with different side chains two possible orientations remain, with one side chain reaching into each of the two adjacent pores. Upon incorporation into an extended lattice, in principle, $2^N$ different relative configurations are possible, in principle. Here we considered two of these configurations (Fig. 3).

In the phase-separated model $ps$-$C_{10}EG_3TA$-COF, all side chains cluster into two types of pores, one with four hydrophobic alkyl chains per pore and another one with four ethylene glycol chains per pore. In this phase-separated configuration, the amphiphilic interactions of the side chains are maximized, which was predicted to be the most energetically favourable
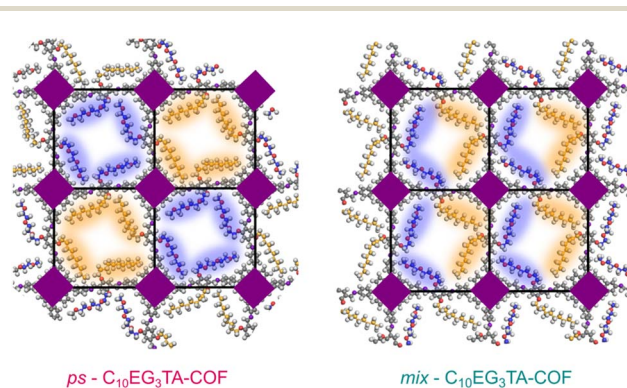


**Fig. 1** Schematic representation of the COF synthesis from a $C_{10}EG_3TA$ functionalized linker and 5,10,15,20-tetrakis(4-aminophenyl)-21$H$,23$H$-porphyrin, showing the formation of $ps$-$C_{10}EG_3TA$-COF, $mix$-$C_{10}EG_3TA$-COF, and other possible configurations depending on the linker arrangement.



**Fig. 3** Schematic representations of the two simulated COF configurations are shown. Nitrogen atoms are highlighted in purple, oxygen in red, carbon atoms of the alkyl chains in orange, and carbon atoms of the EG chains in blue.

This journal is © The Royal Society of Chemistry 2026

*J. Mater. Chem. A*, 2026, **14**, 1647–1656 | **1649**

state.[35] However, during the synthesis, the thermodynamic dissimilarity is attenuated by the solvents used in the synthesis and the thermal fluctuations under synthesis conditions. The opposing state can be considered, where thermal fluctuation led to a random localization of all side chains. In this mixed state (*mix*-C$_{10}$EG$_3$TA-COF) the average pore contains two ethylene glycol side chains and two alkyl side chains.

Simulated PXRD diffractograms based on both models showed that these were nearly indistinguishable by PXRD (Fig. S5). Indeed, both the phase-separated and mixed-pore models resulted in almost identical PXRD patterns, since the observed reflections only changed the relative peak intensities by small amounts and the cell parameters remained constant, in the two scenarios. In the case of ordered phase separation, supercell structures would be expected, but even in the ideal case they would only produce additional reflections of very low intensity. Small angle X-ray diffraction showed no reflections indicative of a supercell (Fig. S4). This indicates that, with the limited crystallinity of COFs and with the relatively similar electron density of the ethylene glycol and the alkyl side chains, powder diffraction alone cannot precisely determine the nature and the spatial arrangement of the side chains within the pores.

Taking this into account, we modelled the structure as a simple "primitive" unit cell with $Z = 1$, corresponding to one porphyrin molecule per unit cell. The initial unit cell parameters were first optimized through force-field geometry optimizations and subsequently refined against the experimental powder diffraction data *via* Pawley refinement ($R_{wp}$: 3.40) (Fig. 2A). The calculated PXRD pattern showed good agreement with the experimental data, resulting in refined unit cell parameters: $a = 25.56$ Å, $b = 25.42$ Å, $c = 4.00$ Å, $\alpha = 67°$, $\beta = 97°$ and $\gamma = 91°$. The symmetry reduction from the tetragonal unit cell was required to explain the split reflection of the 100 and 010 peaks at 0.247 Å$^{-1}$ and 0.267 Å$^{-1}$, respectively. Models with $a \neq b$ and $\alpha = \beta = \gamma = 90°$ also produced good Pawley fits, but led to chemically unreasonably short lattice parameters.

To further analyze and validate the structure of C$_{10}$EG$_3$TA-COF, we performed cryo-TEM. HRTEM images revealed well-defined crystalline domains with a square lattice arrangement in different orientations, clearly confirming the symmetry of the structure (Fig. 2B). Fast Fourier Transform (FFT) analysis of oriented crystallites confirmed spots for *d*-spacings that matched with those derived from the powder X-ray diffraction (PXRD). In particular, the FFT spots that we assigned to 100 and 010 confirmed *d*-spacings of 2.53 nm and 2.32 nm respectively, which align well with values obtained from the Pawley refinement.

The IR spectrum of C$_{10}$EG$_3$TA-COF was analysed (Fig. S7). The characteristic aldehyde (–CHO) vibration at 1679 cm$^{-1}$ that was present in the C$_{10}$EG$_3$TA, mostly disappeared. Concomitantly, the appearance of the imine (–CH=N–) stretch vibration at 1617 cm$^{-1}$ confirmed the conversion of the precursor aldehyde into the COF. The presence of a small residual aldehyde vibration suggests the possible presence of trace amounts of unreacted starting materials or aldehyde-functionalized surface groups on the C$_{10}$EG$_3$TA-COF units, which is known from other COFs.[17,50]

To characterize the porosity and specific surface area of the synthesized COF, nitrogen adsorption–desorption isotherms were measured at 77 K (Fig. S8) showing a BET surface area of 241 m$^2$ g$^{-1}$. The moderate surface area may be attributed to partial pore blocking or filling by the linker side chains, which could limit the full access of nitrogen molecules to the internal pore volume. To further assess the porosity, the pore size distribution was analysed using the non-local density functional theory equilibrium model NLDFT (Fig. S9). The results indicate the predominant micropore centred at 1.4 nm. In addition, minor and broader contributions extending into the mesopore range (more than 3 nm) were attributed to interparticle voids and structural disorder, rather than intrinsic framework porosity of the COF.

### Solid-state NMR (ssNMR)

The chemical composition of the COFs was verified using magic angle spinning (MAS) at 10 kHz solid-state $^{13}$C and $^1$H nuclear magnetic resonance (NMR) spectroscopy. In the $^{13}$C solid-state NMR spectra (Fig. 4A), a distinctive signal at 152.6 ppm indicates the presence of the imine linkage (–CH=N–). Signals at 144.2, 137.1, 127.8, 114.9, and 109.9 ppm are attributed to the aromatic carbons from both the porphyrin core and the aromatic part of the linker, based on assignments derived from literature[51] and solution $^{13}$C NMR (Fig. S16) and HETCOR experiments (Fig. 4B). The MAS $^{13}$C NMR spectra clearly show the presence of distinct sets of signals, confirming the successful integration of dual side chains. Resonances in the range of 62.9–74.5 ppm are characteristic of alkoxy carbons (–C–O–) groups associated with the polyethylene glycol side chain, and also of the carbon atoms linking the central core to both the hydrophilic and hydrophobic moieties (assigned as p and t in Fig. 4A). Multiple peaks between 22.7–32.2 ppm correspond to
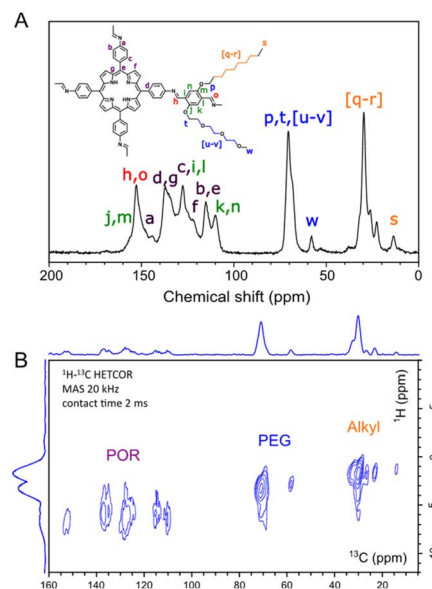


**Fig. 4** (A) Solid-state $^{13}$C CP/MAS NMR spectrum of the COF with carbon signal assignments. (B) $^1$H–$^{13}$C HETCOR spectra showing C–H correlations for the EG, alkyl, and porphyrin units.

**1650** | *J. Mater. Chem. A*, 2026, **14**, 1647–1656

This journal is © The Royal Society of Chemistry 2026

the methylene carbons ($-CH_2-$) of the alkyl chain. The terminal methyl groups $-CH_3$ from the hydrophobic alkyl chain and from the polyethylene glycol chain appear at 12.9 ppm and 57.9 ppm, respectively, labelled as s and w in the spectra (Fig. 4A). In the ssNMR HETCOR ($^1$H–$^{13}$C) experiment (Fig. 4B), the proton spectra reveal two intense, broad peaks centred at 1.52 ppm and 3.59 ppm, corresponding to the aliphatic protons of the hydrophobic chain and the ethylene glycol units of the EG side chain, respectively. An even broader feature can be assigned to aromatic protons of the porphyrin core and the linear linker, characterized by a wide range of chemical shifts centred around 7.38 ppm and partial overlap with the side chain signals (Fig. S17 and S18).

Beyond confirming the successful incorporation of both side chains and overall structural integrity, the well-resolved signals in the $^1$H and $^{13}$C ssNMR spectra enabled a more comprehensive analysis of the material at molecular level. In this study, we established a ssNMR spectroscopy method to directly investigate the presence or absence of phase separation in $C_{10}EG_3TA$-COF, providing insights into the chemical environments within the pores and the spatial arrangement and interactions of the side chains.

To probe these structural aspects, we conducted MAS-based spin-diffusion experiments, which represent the solid-state NMR analogue of solution NOESY experiments, that offer information on through-space interaction of nearby nuclei. The experiments were performed at 10 kHz spinning frequency and 20 °C using the same pulse sequence as for solution-state NOESY. However, in the solid state, magnetization exchange between nuclei occurs *via* spin diffusion, a process dominated by residual dipolar couplings.

The spin diffusion effect relies on a solid-state environment with sufficiently strong homonuclear dipolar couplings among protons, allowing magnetization exchange through flip-flop terms in the dipolar Hamiltonian. These couplings are orientation-dependent and are only partially averaged by molecular motion. In our system, the motion of the side chains, strongly anisotropic, is limited by their covalent attachment to the rigid aromatic framework, maintaining sufficiently strong dipolar interactions. We can therefore assume similar coupling within both side chain types (comparable motional restrictions) and towards the aromatic core. Within the core itself, however, spin diffusion is expected to be even faster due to the higher density of strongly coupled protons typical of rigid aromatic domains.

In different studies, NMR spin diffusion experiments have provided invaluable insights into the nanoscale structure and spatial arrangement of phases in complex polymer systems,[52,53] by analyzing the transfer of spin magnetization between different regions (*e.g.*, rigid, mobile, interphase) can be distinguished based on their distinct molecular mobility, which affects their "transverse relaxation ($T_2$) behavior".[53]

Moreover, in previous studies on metal–organic frameworks with side chains of similar length, we measured residual couplings of several kHz at the side-chain ends, which proved suitable for spin diffusion analysis.[49] In our case, the comparably large integrals observed for side-chain resonances in Fig. 5

proves sufficiently strong dipolar couplings, as 2 ms of cross-polarization *via* $^1$H–$^{13}$C dipolar couplings were sufficient to polarize them to the stoichiometric level. This supports that spin diffusion can efficiently probe structural features in our system.

Consequently, to explore the spin-diffusion network among different protons, we performed 2D $^1$H–$^1$H exchange experiments. The 10 kHz MAS frequency provided a good compromise between sufficient spectral resolution of the well-separated signal regions (framework, EG, and alkyl) and moderate averaging of $^1$H–$^1$H dipolar couplings. As already mentioned before, the pulse sequence is essentially identical to the solution-state NOESY experiment, in which the indirect and direct chemical-shift encoding dimensions are separated by a *z*-filter of variable duration, during which magnetization exchange can occur. The interval, called mixing time, during which magnetization was allowed to mix *via* spin diffusion between the different nuclei was varied as follows: 100 µs, 3 ms, 8 ms, 15 ms, and 25 ms (Fig. 5 and S19).

At the shortest mixing time of 100 µs, magnetization remained confined to the diagonal, indicating that no significant spin diffusion between nuclei had occurred (Fig. 5A). Clear evidence of spin exchange was observed with the appearance of off-diagonal signals (cross peaks) at longer mixing times. At 3 ms and 8 ms, small but clear indications of spin exchange were noted among the two different side chain types (Fig. 5B and C), indicating that EG and alkyl side chains are close enough in space to undergo direct spin diffusion and therefore interact spatially.

These cross peaks became more pronounced at 15 ms and were well resolved by 25 ms (Fig. 5D and S19D, E). Due to the broad nature of the aromatic signals (featuring much stronger dipolar couplings), the cross peaks between the side chain and
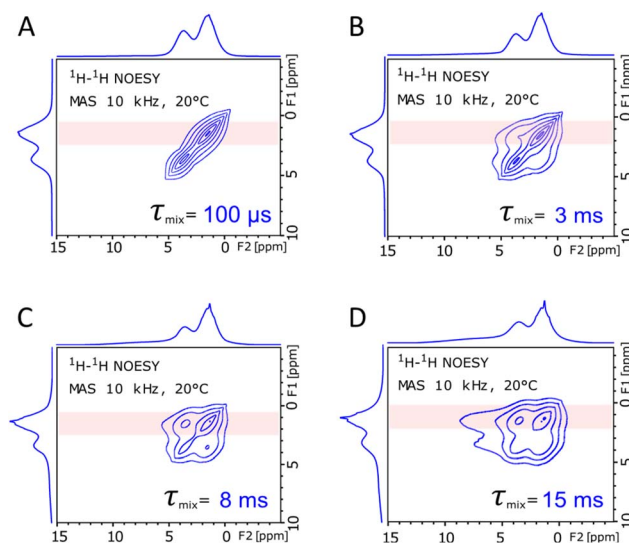


**Fig. 5** 2D $^1$H–$^1$H spin-diffusion spectra at different mixing times ($\tau_{mix}$) under MAS at 10 kHz and a temperature of 20 °C. (A)–(D) show $\tau_{mix}$ values of 100 µs, 3 ms, 8 ms, and 15 ms, respectively. The red–shaded region indicates the integration range along the indirect dimension (along *y*) for the 1D projections shown in Fig. 6A.

This journal is © The Royal Society of Chemistry 2026

*J. Mater. Chem. A*, 2026, **14**, 1647–1656 | **1651**

the aromatic core are also broad and not easily identified in the contour plot. However, they could be clearly identified at the longest mixing times (Fig. 5D and S19D, E).

Critically, the observation that side chain-side chain cross peaks appeared at shortly before or nearly the same rate as side chain-core cross peaks provided compelling evidence against phase separation, where different kind of side chains are segregated into distinct microdomains/pores. Rather, this suggests that the system is not entirely phase separated, indicating a mixed arrangement, where alkyl and EG side chains coexist within the same pores. The appearance of cross peaks at short mixing times between alkyl and EG side chain protons demonstrates their direct close spatial proximity and dynamic interactions.

In a phase-separated scenario, cross peaks between different side chain types would either be absent or weaker within these mixing times or appear only after significantly longer delays, requiring magnetization to cross the aromatic region as an intermediate step.

The polarization transfer between these two types of side chains would necessarily occur indirectly *via* the aromatic framework. The core protons would have to be polarized well before the other side chain type (since only the core protons can be the polarization source for the other type of side chain). One would expect sequential spin diffusion: first from the side chain to the core, and then from the core to the other side chain (Fig. 6C).

For a more quantitative assessment, we calculated 1D sum projections over the chemical-shift region of the aliphatic signals in the indirect dimensions (see the shaded regions in Fig. 5). They more clearly showed how the proton signals changed with increasing mixing time (Fig. 6A). The main peak, attributed to the non-polar alkyl side chain, decreased in intensity over time, while the two other peaks corresponding to the polar EG side chains and the aromatic cores increased at remarkably similar rates. The spectra were accurately fitted using a sum of three Lorentzian curves, allowing the extraction of time dependent signal intensities (corresponding to the area under each peak) resulting in an amplitude plot with one curve for each component (Fig. 6B).

This finding clearly demonstrated that the material is not phase separated, because the protons from the other type of side chain are polarized at the same rate as the core protons. In case side chains were separated and interacted only through a rigid aromatic core, and so the aromatic signal (pink curve) would have to increase significantly more rapidly than the polar side chain (blue curve), which is not observed (Fig. 6B).

Instead, both components exhibited simultaneous increases in intensity, implying direct rather than relayed spin-diffusion pathways and confirming the absence of a spatial barrier between two potential different environments built by the aromatic cores. These results support a homogeneous molecular distribution, in which side chains are spatially mixed and interact directly.

We note that our conclusions are subject to an ambiguity related to the first –OCH$_2$ group in the alkyl chain (labelled "p" in Fig. 4), which resonates in the same ppm range as the EG chain.



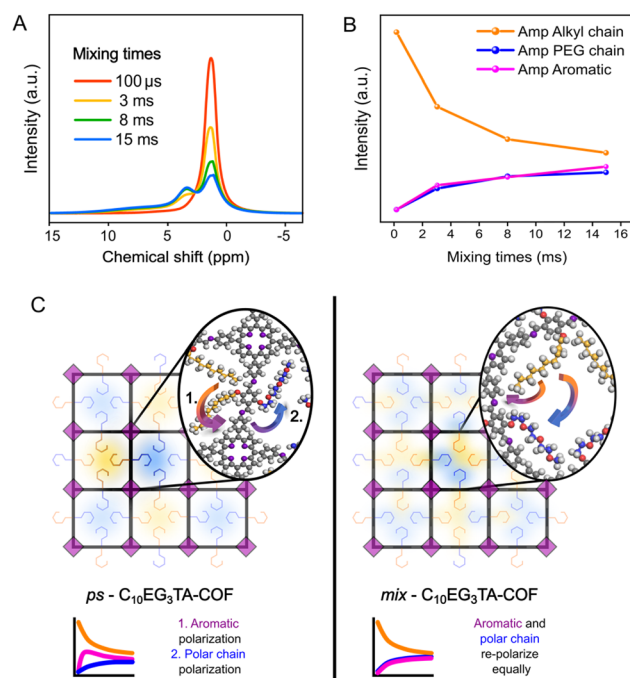**Fig. 6** (A) Projections from 2D $^1$H–$^1$H spin-diffusion ssNMR spectra at different mixing times. (B) Deconvolution results from Lorentzian curves. (C) Schematic representation of the proposed magnetization pathways: pathway A: starting from the alkyl chain, the magnetization crosses the aromatic framework before reaching the EG chain. Pathway B: starting from the alkyl chain the magnetization crosses directly to the EG chain; small insets describe the idealized behavior for pathway A (left) and pathway B (right). In a phase separated situation the pathway A should dominate and the transfer to EG would be delayed, leading to a slower increase of the blue signal compared to the pink one.

This means that some (smaller) part of the magnetization exchange among these groups of protons occurs irrespective of the state of mixing. While we argue that the effect is likely small in relation to the overall proton number in the different side chains, we will address this issue in future work through more quantitative modelling of the NMR results and a wider range of experiments, such as a suppression of the signal of the ambiguous side-chain part *via* a ($T_2$) filter before detection.

### Computational analysis

The relative stability of the two COF configurations was investigated through density functional theory (DFT) calculations to identify the energetically most favourable arrangement (Fig. S20). These simulations were performed without considering for temperature effects or solvent-mediated interactions during crystallization. Since such factors could play an important role in modulating the enthalpic contributions and the overall free energy of mixing, they will be taken in consideration in consecutive and complementary studies.

Three specific cases were evaluated. In the first one, corresponding to the phase-separated *ps* configuration, the layers adopt an AA stacking mode in which chains of the same chemical nature are next to each other in the stacking direction and within the pore. In the mixed scenario we differentiated two

cases: *mix*-1, where a pore in each layer contains two polar and two alkyl side chains, and also the same type of chains are found along the stacking direction. *mix*-2, where the chains differ along the stacking direction, leading to intimate contact of polar *vs.* alkyl chains.

The relative energies were calculated using the formula $\Delta E = E_{MIX} - E_{PS}$, yielding energy differences of 0.00 eV (0.00 kcal mol$^{-1}$) per unit cell for the first configuration, 0.13 eV (3.00 kcal mol$^{-1}$) for the second, and 5.96 eV (137.44 kcal mol$^{-1}$) for the third system. These results indicate that the *ps* configuration is slightly more favourable than the *mix*-1, and significantly more stable than the third arrangement (*mix*-2). All calculations were performed considering four porphyrin units and sixteen side chains (eight ethylene glycol and eight alkyl) per unit cell, the calculated relative energy differences are very small per atom.

From an enthalpic perspective, these findings are consistent with our initial hypothesis and with what was reported by Ji *et al.* Moreover, they confirm that there is no strong energetic preference between the *ps* and *mix* configurations, suggesting that mixed arrangements are indeed accessible under experimental conditions. This analysis therefore supports our interpretation that the mixed configuration is energetically plausible.

## Discussion

These findings are in contrast with expectations for a phase-separated system that Ji *et al.* proposed for a closely related COF.[35] In the work by Ji *et al.*, shorter side chains were used with a diethylene glycol and heptyl side chains, which are both shorter than the triethylene glycol and decyl side chains used in this work (Fig. 7). The use of longer side chains is expected to further promote phase separation for two reasons: (1) longer side chains increase the interactions across the pore and with next neighbours since the region of overlap between side chains is increased; (2) longer chains tend to have stronger phase separation tendency due to decreasing entropy of mixing with increased lengths, leading to enthalpic/"philic" interactions dominating. Additionally, the linear linker based on a terphenyl core is much longer than the phenyl based linear linker reported here. This leads to much smaller pores in our system and thereby again increased interchain interactions for geometric reasons.

Another factor that makes both COFs comparable is the similar synthesis conditions: 9 : 1 : 2 *o*-dichlorobenzene/ ethanol/aq. acetic acid (6 M) *vs.* 9 : 1 : 1 *o*-dichlorobenzene/*n*-butanol/aq. acetic acid (6 M) in our system, reacted at 120 °C for 3 days.
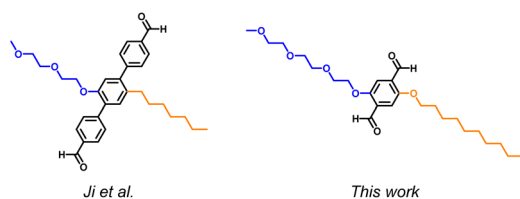


**Fig. 7** Comparison of the amphiphilic linker used by Ji *et al.*[35] and the linker used in this work.

The direct evidence from ssNMR showing that hydrophilic and hydrophobic side chains are intermixed in our COF, combined with additional factors that should promote phase separation in our system, suggests that previously reported amphiphilic COFs are also unlikely to exhibit true phase separation. However, since these systems differ in molecular design and synthetic conditions, definitive conclusions can only be drawn through direct experimental investigation of each material.

Beyond these insights, our study opens new perspectives for the rational design of COFs with chemically heterogeneous porosity. Now that we have demonstrated ssNMR to be an essential tool for explaining molecular-level organization in porous materials, it becomes equally important to guide the synthesis toward systems that actively favour phase separation. This may involve the introduction of fluorinated or longer side chains, incorporation of ionic or hydrogen-bonding functionalities, and systematic variation of solvent conditions or temperature during synthesis.[54,55]

Future developments may also include quantitative characterization of the mobility *via* $^1$H–$^{13}$C dipolar couplings DI-PSHIFT NMR of the side chains,[49] structural refinement through NMR crystallography supported by theoretical predictions,[56] and examinations of guest/solvent–pore interactions and guest dynamics utilizing advanced ssNMR techniques.

## Methods

### High-resolution synchrotron X-ray diffraction and total scattering

Measurements were conducted at beamline ID31 at the European Synchrotron Radiation Facility (ESRF). Sample was loaded into cylindrical slots between Kapton windows. The experiment was done in a transmission with an incident X-ray energy of 75.00 keV ($\lambda = 0.01653$ nm). Intensity data was collected using a Pilatus CdTe 2M detector with a sample-to-detector distance of 1.5 m. Background data was subtracted, and geometry calibration was performed with NIST SRM 660b (LaB$_6$) using pyFAI software. SAXS measurements were performed with a Perkin-nElmer detector at 8.9 m, using a flight tube to reduce air scattering.

### Structure building and conformation analysis

BIOVA Materials Studio 2022 Dassault Systémes was used to build and simulated the unit cells and to perform geometry optimizations using the universal force field.

### Refinement

The PXRD pattern was analyzed by Pawley refinement using TOPAS Academic and the resulting cell parameters were used as initial values for the simulated structures.

### TEM

Approximately 2 mg of the COF sample was dispersed in 200 μL of ethanol and sonicated for 10 minutes to ensure uniform suspension. The dispersion was then centrifuged at 1000g for 5

minutes. A 3.5 μL aliquot of the resulting supernatant was deposited onto the carbon-coated side of lacey carbon grids. Excess liquid was gently wicked away from the reverse side using filter paper, and the grids were allowed to air-dry. The prepared grids were mounted onto a Thermo Fisher Autogrid assembly and introduced into a Thermo Fisher Scientific Glacios cryogenic electron microscope at ambient temperature. Specimens were equilibrated overnight under vacuum within the instrument's autoloader before being cooled to cryogenic temperatures. Low-dose imaging was carried out at a nominal magnification of 150 000×, corresponding to a calibrated pixel size of 0.936 Å. Data were acquired in electron counting mode using a Falcon 4i direct electron detector at a total exposure dose of 50 e⁻ per Å². To minimize the beam-induced sample drift, all images were motion-corrected and saved as integrated single frames.

### Computational setup

Atomistic calculations were carried out within the framework of density functional theory (DFT). We evaluated the total energy of three crystalline configurations of the same COF, which share the same molecular building units but differ in the orientation and arrangement of the linker side chains within the pores and stacking of the layers. The energies were compared after a slight geometry refinement *via* DFT optimization using the BFGS-optimizer.[57] All simulations were performed using the CP2K software package.[58] The electronic wavefunctions were expanded in a double-zeta valence plus polarization (DZVP-MOLOPT) basis set[59] optimized for molecular systems, in combination with Goedecker–Teter–Hutter (GTH) pseudopotentials.[60] Exchange–correlation effects were treated using the generalized gradient approximation (GGA) with the Perdew–Burke–Ernzerhof (PBE) functional,[61] complemented by the DFT-D3 dispersion correction scheme[62] to account for long-range van der Waals interactions.

### Solid-state NMR

Solid state NMR experiments were performed on a Bruker NEO spectrometer with the proton resonance frequency 400 MHz using 4 mm MAS probe. ¹H 90° pulse duration was 3 μs, contact time in ¹³C CPMAS and ¹H–¹³C HETCOR experiments was 1.5 ms. For proton dipolar decoupling 80 kHz spinal sequence was applied. Number of accumulations was 4000 for the ¹³C CPMAS, 256 for ¹H–¹³C HETCOR, and 16 for ¹H–¹H spin-diffusion experiments. Number of increments in the indirect dimension was 400 and 40 in ¹H–¹H spin-diffusion and ¹H–¹³C HETCOR experiments, respectively. All measurements were conducted at sample temperature 20 °C, which was achieved using precooling of VT gas.

## Conclusions

Our results demonstrate that solid-state NMR (ssNMR) spectroscopy is a powerful and direct technique for probing the molecular organization within amphiphilic covalent organic frameworks (COFs). By synthesizing a square-lattice COF from a linear amphiphilic linker and a tetrafunctional porphyrin tetraamine node (TAPP), we obtained a system with small, uniform pores designed to promote side chain interactions and potential microphase separation. 2D ¹H–¹H spin-diffusion ssNMR spectra clearly demonstrated that the side chains are present in this COF in a mixed single phase and are not phase separated. This surprising result calls into question whether phase separation does occur in other systems, with larger pore sizes and shorter side chains, which would lead to even fewer side chain interactions that promote phase separation. Nevertheless, this direct evidence of the local side chain organization now allows for further studies into the synthesis parameters and other linker systems to search for phase separated amphiphilic COFs and unambiguously prove their phase separation.

## Conflicts of interest

There are no conflicts to declare.

## Data availability

All relevant experimental data are included in the manuscript and the supplementary information (SI). Supplementary information: detailed methods, SAXS data, structural simulations, NMR spectra, N₂ sorption, synthesis of the linker molecules and materials. See DOI: https://doi.org/10.1039/d5ta06558e.

## Acknowledgements

1654 | *J. Mater. Chem. A*, 2026, **14**, 1647–1656

This journal is © The Royal Society of Chemistry 2026

# Notes and references

1 P. J. Waller, F. Gándara and O. M. Yaghi, *Acc. Chem. Res.*, 2015, **48**, 3053–3063.

2 F. Haase, T. Banerjee, G. Savasci, C. Ochsenfeld and B. V. Lotsch, *Faraday Discuss.*, 2017, **201**, 247–264.

3 M. Lu, M. Zhang, J. Liu, Y. Chen, J. Liao, M. Yang, Y. Cai, S. Li and Y. Lan, *Angew. Chem., Int. Ed.*, 2022, **61**, e202200003.

4 M. Xiao, Y. Wei and R. Yu, *ChemNanoMat*, 2023, **9**, e202200408.

5 K. Zhang, L. Zhou, Z. Wang, H. Li, Y. Yan and J. Zhang, *Phys. Chem. Chem. Phys.*, 2022, **24**, 23690–23698.

6 X. Tian, L. Cao, K. Zhang, R. Zhang, X. Li, C. Yin and S. Wang, *Angew. Chem., Int. Ed.*, 2025, **64**, e202416864.

7 H. Li, J. Chang, S. Li, X. Guan, D. Li, C. Li, L. Tang, M. Xue, Y. Yan, V. Valtchev, S. Qiu and Q. Fang, *J. Am. Chem. Soc.*, 2019, **141**, 13324–13329.

8 Y. Yusran, H. Li, X. Guan, D. Li, L. Tang, M. Xue, Z. Zhuang, Y. Yan, V. Valtchev, S. Qiu and Q. Fang, *Adv. Mater.*, 2020, **32**, 1907289.

9 X. Liu, H. Pang, X. Liu, Q. Li, N. Zhang, L. Mao, M. Qiu, B. Hu, H. Yang and X. Wang, *Innovation*, 2021, **2**, 100076.

10 S. Zhang, D. Liu and G. Wang, *Molecules*, 2022, **27**, 2586.

11 F. Rastegari, S. Asghari, I. Mohammadpoor-Baltork, H. Sabzyan, S. Tangestaninejad, M. Moghadam and V. Mirkhani, *J. Hazard. Mater.*, 2024, **476**, 135075.

12 F. Mehvari, V. Ramezanzade, P. Asadi, N. Singh, J. Kim, M. Dinari and J. S. Kim, *Aggregate*, 2024, **5**, e480.

13 F. Haase and B. V. Lotsch, *Chem. Soc. Rev.*, 2020, **49**, 8469–8500.

14 C. G. Gruber, L. Frey, R. Guntermann, D. D. Medina and E. Cortés, *Nature*, 2024, **630**, 872–877.

15 Y. Li, J. Sui, L.-S. Cui and H.-L. Jiang, *J. Am. Chem. Soc.*, 2023, **145**, 1359–1366.

16 S. Kandambeth, D. B. Shinde, M. K. Panda, B. Lukose, T. Heine and R. Banerjee, *Angew. Chem., Int. Ed.*, 2013, **52**, 13052–13056.

17 A. Winter, F. Hamdi, A. Eichhöfer, K. Saalwächter, P. L. Kastritis and F. Haase, *Chem. Sci.*, 2024, **15**, 14449–14457.

18 W. A. Braunecker, K. E. Hurst, K. G. Ray, Z. R. Owczarczyk, M. B. Martinez, N. Leick, A. Keuhlen, A. Sellinger and J. C. Johnson, *Cryst. Growth Des.*, 2018, **18**, 4160–4166.

19 S. B. Alahakoon, S. D. Diwakara, C. M. Thompson and R. A. Smaldone, *Chem. Soc. Rev.*, 2020, **49**, 1344–1356.

20 S. D. Diwakara, W. S. Y. Ong, Y. H. Wijesundara, R. L. Gearhart, F. C. Herbert, S. G. Fisher, G. T. McCandless, S. B. Alahakoon, J. J. Gassensmith, S. C. Dodani and R. A. Smaldone, *J. Am. Chem. Soc.*, 2022, **144**, 2468–2473.

21 F. Haase, K. Gottschling, L. Stegbauer, L. S. Germann, R. Gutzler, V. Duppel, V. S. Vyas, K. Kern, R. E. Dinnebier and B. V. Lotsch, *Mater. Chem. Front.*, 2017, **1**, 1354–1361.

22 S. B. Alahakoon, K. Tan, H. Pandey, S. D. Diwakara, G. T. McCandless, D. I. Grinffiel, A. Durand-Silva, T. Thonhauser and R. A. Smaldone, *J. Am. Chem. Soc.*, 2020, **142**, 12987–12994.

23 Z.-F. Pang, T.-Y. Zhou, R.-R. Liang, Q.-Y. Qi and X. Zhao, *Chem. Sci.*, 2017, **8**, 3866–3870.

24 C. E. Pelkowski, A. Natraj, C. D. Malliakas, D. W. Burke, M. I. Bardot, Z. Wang, H. Li and W. R. Dichtel, *J. Am. Chem. Soc.*, 2023, **145**, 21798–21806.

25 X. Li, P. Yadav and K. P. Loh, *Chem. Soc. Rev.*, 2020, **49**, 4835–4866.

26 Y. Kong, B. Lyu, C. Fan, Y. Yang, X. Wang, B. Shi, J. Jiang, H. Wu and Z. Jiang, *J. Am. Chem. Soc.*, 2023, **145**, 27984–27992.

27 J. Yang, L. Li and Z. Tang, *Matter*, 2021, **4**, 2666–2668.

28 Z. Xie, X. Chen, W. Wang, X. Ke, X. Zhang, S. Wang, X. Wu, J. C. Yu and X. Wang, *Angew. Chem., Int. Ed.*, 2024, **63**, e202410179.

29 S. Sun, C.-Q. Han, J.-X. Guo, L. Wang, Z.-Y. Wang, G. Lu and X.-Y. Liu, *J. Mater. Chem. C*, 2025, **13**, 2814–2821.

30 A. De, S. Haldar, S. Michel, L. Shupletsov, V. Bon, N. Lopatik, L. Ding, L. M. Eng, G. K. Auernhammer, E. Brunner and A. Schneemann, *Chem. Mater.*, 2023, **35**, 3911–3922.

31 H. Wang, Y. Zhai, Y. Li, Y. Cao, B. Shi, R. Li, Z. Zhu, H. Jiang, Z. Guo, M. Wang, L. Chen, Y. Liu, K.-G. Zhou, F. Pan and Z. Jiang, *Nat. Commun.*, 2022, **13**, 7123.

32 M. Wu, Y. Zhu and W. Jiang, *Angew. Chem., Int. Ed.*, 2018, **57**, 3578–3582.

33 J. Chu, Y. Lu, S. Gan, Q. Qi, C. Jia, J. Yao and X. Zhao, *Macromol. Rapid Commun.*, 2023, **44**, 2200641.

34 Q. Sun, B. Aguila, P. C. Lan and S. Ma, *Adv. Mater.*, 2019, **31**, 1900008.

35 W. Ji, P. Zhang, G. Feng, Y.-Z. Cheng, T.-X. Wang, D. Yuan, R. Cha, X. Ding, S. Lei and B.-H. Han, *Nat. Commun.*, 2023, **14**, 6049.

36 S.-Y. Jiang, Z.-B. Zhou, S.-X. Gan, Y. Lu, C. Liu, Q.-Y. Qi, J. Yao and X. Zhao, *Nat. Commun.*, 2024, **15**, 698.

37 C. Anders, V.-M. Fischer, T. Tan, M. Alaasar, R. Waldecker, Y. Ke, Y. Cao, F. Liu and C. Tschierske, *J. Mater. Chem. C*, 2025, **13**, 37–53.

38 C. Wang, Z. Wang and X. Zhang, *Acc. Chem. Res.*, 2012, **45**, 608–618.

39 D. Lombardo, M. A. Kiselev, S. Magazù and P. Calandra, *Adv. Condens. Matter Phys.*, 2015, **2015**, 1–22.

40 S. U. Rehman, S. Xu, H. Xu, T. Tao, Y. Li, Z. Yu, K. Ma, W. Xu and J. Wang, *Mater. Today Adv.*, 2022, **16**, 100287.

41 M. Zheng, Y. Chu, Q. Wang, Y. Wang, J. Xu and F. Deng, *Prog. Nucl. Magn. Reson. Spectrosc.*, 2024, **140–141**, 1–41.

42 C. He, S. Li, Y. Xiao, J. Xu and F. Deng, *Solid State Nucl. Magn. Reson.*, 2022, **117**, 101772.

43 S. Li, O. Lafon, W. Wang, Q. Wang, X. Wang, Y. Li, J. Xu and F. Deng, *Adv. Mater.*, 2020, **32**, 2002879.

44 B. E. G. Lucier, S. Chen and Y. Huang, *Acc. Chem. Res.*, 2018, **51**, 319–330.

45 H. Hoffmann, M. Debowski, P. Müller, S. Paasch, I. Senkovska, S. Kaskel and E. Brunner, *Materials*, 2012, **5**, 2537–2572.

This journal is © The Royal Society of Chemistry 2026

*J. Mater. Chem. A*, 2026, **14**, 1647–1656 | **1655**

46 *NMR of Metal–Organic Frameworks and Covalent Organic Frameworks*, ed. W. Wang, S. Chen and Y. Huang, Royal Society of Chemistry, 2024.

47 A. J. Rossini, A. Zagdoun, M. Lelli, J. Canivet, S. Aguado, O. Ouari, P. Tordo, M. Rosay, W. E. Maas, C. Copéret, D. Farrusseng, L. Emsley and A. Lesage, *Angew. Chem., Int. Ed.*, 2012, **51**, 123–127.

48 C. Franz, F. Lange, Y. Golitsyn, B. Hartmann-Azanza, M. Steinhart, M. Krutyeva and K. Saalwächter, *Macromolecules*, 2016, **49**, 244–256.

49 G. Hempel, R. Kurz, S. Paasch, K. Saalwächter and E. Brunner, *Magn. Reson.*, 2024, **5**, 1–20.

50 F. Haase, E. Troschke, G. Savasci, T. Banerjee, V. Duppel, S. Dörfler, M. M. J. Grundei, A. M. Burow, C. Ochsenfeld, S. Kaskel and B. V. Lotsch, *Nat. Commun.*, 2018, **9**, 2600.

51 L.-G. Ding, B.-J. Yao, W.-X. Wu, Z.-G. Yu, X.-Y. Wang, J.-L. Kan and Y.-B. Dong, *Inorg. Chem.*, 2021, **60**, 12591–12601.

52 F. Mellinger, M. Wilhelm and H. W. Spiess, *Macromolecules*, 1999, **32**, 4686–4691.

53 M. Roos, K. Schäler, A. Seidlitz, T. Thurn-Albrecht and K. Saalwächter, *Colloid Polym. Sci.*, 2014, **292**, 1825–1839.

54 N. P. Young and N. P. Balsara, in *Encyclopedia of Polymeric Nanomaterials*, ed. S. Kobayashi and K. Müllen, Springer Berlin Heidelberg, Berlin, Heidelberg, 2014, pp. 1–7.

55 R. Mezzena, B. Pettersson and J.-A. E. Månson, *Polym. Bull.*, 2001, **46**, 419–426.

56 M. Fritzsche, A. Bohle, D. Dudenko, U. Baumeister, D. Sebastiani, G. Richardt, H. W. Spiess, M. R. Hansen and S. Höger, *Angew. Chem., Int. Ed.*, 2011, **50**, 3030–3033.

57 R. Fletcher, *Comput. J.*, 1970, **13**(3), 317–322.

58 T. D. Kühne, M. Iannuzzi, M. Del Ben, V. V. Rybkin, P. Seewald, F. Stein, T. Laino, R. Z. Khaliullin, O. Schütt, F. Schiffmann, D. Golze, J. Wilhelm, S. Chulkov, M. H. Bani-Hashemian, V. Weber, U. Borštnik, M. Taillefumier, A. S. Jakobovits, A. Lazzaro, H. Pabst, T. Müller, R. Schade, M. Guidon, S. Andermatt, N. Holmberg, G. K. Schenter, A. Hehn, A. Bussy, F. Belleflamme, G. Tabacchi, A. Glöß, M. Lass, I. Bethune, C. J. Mundy, C. Plessl, M. Watkins, J. VandeVondele, M. Krack and J. Hutter, *J. Chem. Phys.*, 2020, **152**, 194103.

59 J. VandeVondele and J. Hutter, *J. Chem. Phys.*, 2007, **127**, 114105.

60 S. Goedecker, M. Teter and J. Hutter, *Phys. Rev. B: Condens. Matter Mater. Phys.*, 1996, **54**, 1703–1710.

61 A. V. Terentjev, L. A. Constantin and J. M. Pitarke, *Phys. Rev. B*, 2018, **98**, 214108.

62 S. Grimme, J. Antony, S. Ehrlich and H. Krieg, *J. Chem. Phys.*, 2010, **132**, 154104.

**1656** | *J. Mater. Chem. A*, 2026, **14**, 1647–1656

This journal is © The Royal Society of Chemistry 2026